Smart Structures and Systems, *Vol. 17, No. 3 (2016) 363-389*
DOI: http://dx.doi.org/10.12989/sss.2016.17.3.363

Mode identifiability of a cable-stayed bridge under different excitation conditions assessed with an improved algorithm based on stochastic subspace identification

Wen-Hwa Wu[*1], Sheng-Wei Wang[2a], Chien-Chou Chen[1b] and Gwolong Lai[1c]

[1]*Department of Construction Engineering, National Yunlin University of Science and Technology, 123 University Road, Touliu, Yunlin 640, Taiwan*
[2]*Graduate School of Engineering Science and Technology, National Yunlin University of Science and Technology, 123 University Road, Touliu, Yunlin 640, Taiwan*

(Received May 31, 2015, Revised August 8, 2015, Accepted August 19, 2015)

Abstract. Deficient modes that cannot be always identified from different sets of measurement data may exist in the application of operational modal analysis such as the stochastic subspace identification techniques in large-scale civil structures. Based on a recent work using the long-term ambient vibration measurements from an instrumented cable-stayed bridge under different wind excitation conditions, a benchmark problem is launched by taking the same bridge as a test bed to further intensify the exploration of mode identifiability. For systematically assessing this benchmark problem, a recently developed SSI algorithm based on an alternative stabilization diagram and a hierarchical sifting process is extended and applied in this research to investigate several sets of known and blind monitoring data. The evaluation of delicately selected cases clearly distinguishes the effect of traffic excitation on the identifiability of the targeted deficient mode from the effect of wind excitation. An additional upper limit for the vertical acceleration amplitude at deck, mainly induced by the passing traffic, is subsequently suggested to supplement the previously determined lower limit for the wind speed. Careful inspection on the shape vector of the deficient mode under different excitation conditions leads to the postulation that this mode is actually induced by the motion of the central tower. The analysis incorporating the tower measurements solidly verifies this postulation by yielding the prevailing components at the tower locations in the extended mode shape vector. Moreover, it is also confirmed that this mode can be stably identified under all the circumstances with the addition of tower measurements. An important lesson learned from this discovery is that the problem of mode identifiability usually comes from the lack of proper measurements at the right locations.

Keywords: stochastic subspace identification; cable-stayed bridge; mode identifiability; alternative stabilization diagram; hierarchical sifting process

*Corresponding author, Professor, E-mail: wuwh@yuntech.edu.tw
[a] Ph.D. Student, E-mail: g9710816@yuntech.edu.tw
[b] Associate Professor, E-mail: ccchen@yuntech.edu.tw
[c] Associate Professor, E-mail: laig@yuntech.edu.tw

http://www.techno-press.org/?journal=sss&subpage=8 ISSN: 1738-1584 (Print), 1738-1991 (Online)

1. Introduction

With recent advancement in relating technologies, modal identification of civil engineering structures based on ambient vibration measurements has been commonly adopted for structural health monitoring and damage detection. In such applications where simply the output signals are available, operation modal analysis is necessary for effectively obtaining the modal frequencies, damping ratios, and mode shape vectors. Over the past few decades, several output-only modal identification methods have been developed via the analysis either in the frequency domain or the time domain. The principal frequency domain techniques contain the peak-picking method (Bendat and Piersol 1986), the frequency domain decomposition method (Brinker *et al*. 2001, Jacobsen *et al*. 2006), and the maximum likelihood identification (Parloo *et al*. 2003). The time domain approaches include the eigensystem realization algorithm (Juang and Pappa 1985), the auto regressive moving average model (Ljung 1987), and the stochastic subspace identification (SSI) (Van Overschee and De Moor 1996, Peeters and De Roeck 1999), to name but a few.

Among all these output-only identification methods, SSI has been gaining more popularity in recent years due to its strict mathematical basis and excellent applicability in various systems. The widely employed formulation of SSI was first suggested by Van Overschee and De Moor (1991) and the corresponding algorithm for modal parameter identification was also established by them in the subsequent few years (Van Overschee and De Moor 1993, 1996). A number of core techniques in linear algebra such as RQ (or LQ) decomposition, singular value decomposition (SVD), and oblique projection were utilized in their theoretical derivation and solution algorithm. Because of directly processing the output matrix from measurements, this series of methods are typically referred as the data-driven SSI. In addition to the data-driven SSI, the other type of covariance-driven SSI was initially proposed by Peeters (2000) to conduct SSI with the covariance matrix of output measurements. The covariance-driven SSI is relatively simple in mathematical derivation and generally efficient in computation since it only involves with SVD. Even with the help of stabilization diagram, appropriate discrimination criteria according to theories like clustering analysis (Scionti and Lanslots 2005, Carden and Brownjohn 2008, Alicioglu and Lus 2008, Bakir 2011) need to be further established such that systematic extraction of effective physical modes can be attained to reach the ultimate goal of an automated SSI analysis (Reynders *et al*. 2012, Ubertini *et al*. 2013).

The application of operational modal analysis such as the SSI techniques in large-scale civil structures, however, still encounters difficulties under certain circumstances. For instance, deficient modes that cannot be identified all the time from different sets of measurement data may exist. Even for the cases where the identification of these deficient modes is feasible, the obtained modal parameters can be relatively diversified in comparison to the other robust modes. Such inconsistent results may seriously deteriorate the reliability of the subsequent damage detection using an on-line structural health monitoring (SHM) system to conduct automatic modal identification. Therefore, it is extremely important to validate the fidelity of the identified modal parameters for these deficient modes before they are exploited in vibration-based damage detection. Nevertheless, there is no theoretical or even empirical criterion available for the identifiability of modes in performing the operational modal analysis with ambient vibration measurements. Making use of the long-term monitoring data of ambient vibration responses acquired from the instrumented Ting Kau Bridge (TKB) in Hong Kong under different wind excitation conditions, Ni *et al*. (2015) started a pioneering work in probing the mode identifiability with the data-driven SSI algorithm. It was discovered that a deficient mode is identifiable with

consistent mode shape vectors under typhoon conditions, but not identifiable under weak wind conditions. Furthermore, a threshold value of mean hourly wind speed (7.5 m/sec) was obtained to ensure a reliable identification of this deficient mode. Based on this work, a SHM benchmark problem is launched by taking TKB as a test bed to provide an open platform that will help to further intensify the exploration of mode identifiability.

Attempting to attack the problem that the application of conventional SSI techniques to identify the modal parameters of a stay cable usually leads to a failure, a recent work by the authors (Wu *et al*. 2014, 2016) established an improved algorithm based on the covariance-driven SSI. An alternative stabilization diagram was first proposed to more conveniently stand out stable modal parameters and a hierarchical sifting process was then developed to systematically extract reliable modal parameters from the alternative stabilization diagram. Demonstrated by analyzing the ambient vibration measurements of real stay cables, the feasibility of this new approach was verified with successfully obtaining the modal frequencies, damping ratios, and mode shape ratios for almost all the cable modes in the examined frequency range. Equipped with this improved SSI algorithm, the current study aims to extensively assess the aforementioned benchmark problem of mode identifiability by delving into its mechanism behind. A preliminary analysis of known data sets is first conducted to recognize the importance of considering the traffic excitations along with the wind excitations, followed by analyzing the known and blind data sets under different excitation conditions with the improved SSI algorithm to postulate a vibration mechanism for the targeted deficient mode. Finally, the measurements at the central tower are further incorporated in the SSI analysis for directly verifying this mechanism deduced from the deck measurements.

2. Ting Kau Bridge, its sensor deployment and description of investigated data sets

2.1 Ting-Kau Bridge

Ting Kau Bridge, as shown in Fig. 1, is a thee-tower cable-stayed bridge connecting Tsing Yi and Ting Kau located in Hong Kong. It consists of two main spans (448 m+475 m) and two side spans (127 m+127 m) to have a total length of 1177 m. In the transverse direction, the deck is supported at the three towers, the pier at the Ting Kau end, and the abutment at the Tsing Yi end. Moreover, the deck is merely restrained at the central tower in the longitudinal direction. The three slender single-column towers of TKB are with heights of 170 m (Ting Kau Tower), 194 m (Central Tower), and 158 m (Tsing Yi Tower), respectively. The cable system is arranged in four planes and all the 384 stay cables are anchored to the deck edge girders at 13.5 m intervals. Eight longitudinal stabilizing cables, up to 464.6 m long and diagonally connecting the top of the central tower to the deck adjacent to side towers, are designed to restrain the central tower from traffic and vertical wind loading.

2.2 Sensor setup

After the completion of TKB in 1999, a long-term system has been devised by the Highways Department of the Hong Kong SAR Government to monitor the structural health and performance of this bridge (Wong 2004, Ko and Ni 2005). The sensors permanently installed on TKB include 45 accelerometers, 7 anemometers, 2 displacement transducers, 83 temperature sensors, 88 strain gauges and 6 weigh-in-motion sensors (Wong 2007, Ni *et al*. 2011). In this subsection, description

will only cover the deployment of the accelerometers and anemometers related to the measurements adopted in the current study.

As illustrated in Fig. 1, there are three propeller-type anemometers installed at the top of each tower. Besides, four ultrasonic-type anemometers were installed on both sides of the deck at Sections E and L. The sampling frequency of all the anemometers was set at 2.56Hz. Fig. 1 also displays that a total of 24 uni-axial accelerometers were employed to measure the vibration signals at eight deck sections of TKB. Furthermore, four bi-axial accelerometers were used to record the acceleration histories at the top of each tower and at the base of central tower. The detailed arrangement of the accelerometers installed on the bridge deck is plotted in Fig. 2. It should be noted that the accelerometers (2, 5, 8, 11, 14, 17, 20, and 23) installed along the central line of deck measure the transverse (*y*-direction) acceleration and those (1, 3, 4, 6, 7, 9, 10, 12, 13, 15, 16, 18, 19, 21, 22, and 24) installed at both sides of deck collect the vertical (*z*-direction) response. The sampling frequency of all the accelerometers was set at 25.6Hz.

2.3 Description of investigated data sets

In this benchmark study on mode identifiability, 13 sets of 1-hour acceleration records collected from the 24 accelerometers deployed on the bridge deck in 1999 are adopted as known data. Based on the associated mean hourly wind speed calculated with the data from the anemometers located on the windward side of the deck (Ni *et al*. 2015), these known data sets can be classified into three different wind excitation conditions. As listed in Table 1, 6 sets are under the normal (weak) wind condition with their mean hourly speeds all less than 7.5 m/sec and will be referred as Cases N1 to N6. On the other hand, 4 sets are under the typhoon (strong) wind condition with their mean hourly speeds far beyond 7.5 m/sec and will be labeled with the names of their corresponding typhoons. Moreover, 3 critical cases are with their mean hourly wind speeds in the neighborhood of 7.5 m/sec and will be denoted by Cases C1 to C3. In addition to the 13 known data sets, the 6 other sets of 1-hour monitoring acceleration data without given wind excitation conditions are also provided in the benchmark study as blind data. The blind datasets includes 2 sets of data under the weak wind excitation, 2 sets under the typhoon excitation, and 2 sets under the critical condition. These blind data will be used to verify the methodology established in this work.

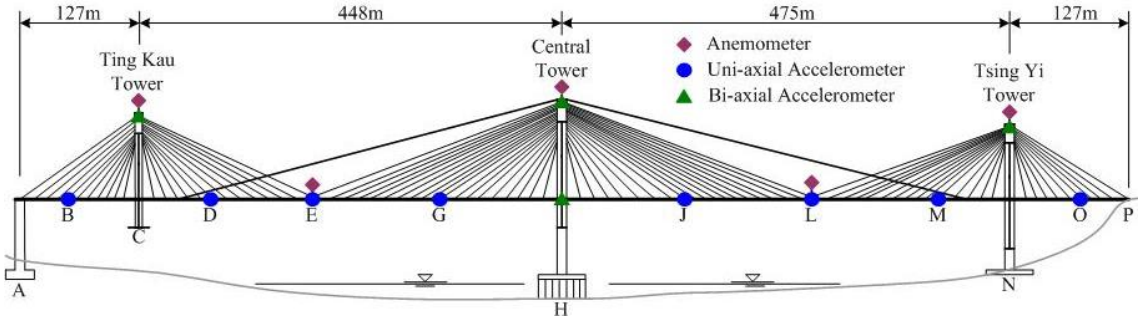

Fig. 1 Ting Kau Bridge and its sensor locations

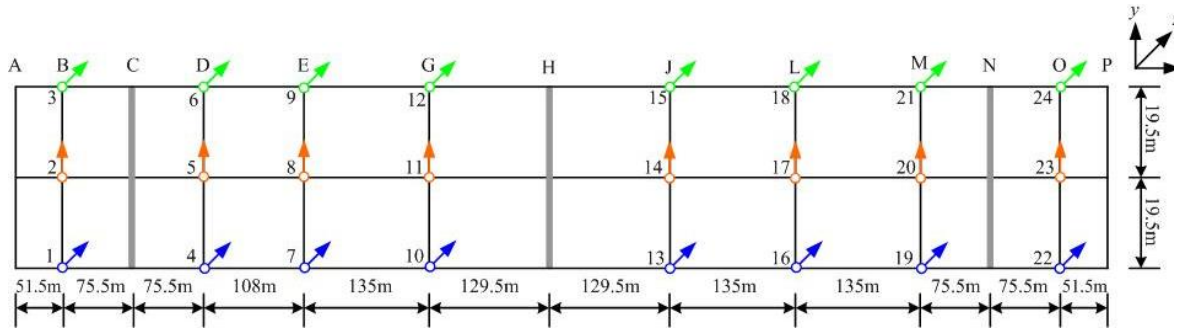

Fig. 2 Detailed arrangement of accelerometers on bridge deck

3. Preliminary analysis of known data sets

Before assessing the mode identifiability problem with the improved SSI algorithm, a preliminary analysis is first performed on the known data sets to assemble more vibration characteristics of TKB under different excitation conditions. The acceleration records of Sensors 10 and 11 located at Section G are examined herein to represent the vertical and transverse responses of bridge deck, respectively. Case N1 under weak wind condition, Case Sam under strong wind condition, and Case C2 under critical wind condition are taken for illustrating three distinctive wind excitations. Figs. 3 and 4 depict the corresponding time histories and Fourier amplitude spectra (FAS), respectively. From Fig. 3, it is clear that the vertical response is generally larger than the transverse response at the deck of TKB. More importantly, both the vertical and transverse responses of Case N1 are much greater than the corresponding quantities of the other two cases. This phenomenon apparently indicates that the deck response is mainly induced by the passing traffic. Under the typhoon or critical conditions, the traffic is certainly decreased or even restricted such that the deck vibration is significantly reduced. The FAS in Fig. 4 over the low frequency range from 0 to 0.5 Hz further discloses the identifiability for the first few major modes of bridge deck under different excitation conditions. First of all, the mode with a frequency of 0.165 Hz is dominant in the vertical FAS under all the excitation cases. This mode has been identified as the first vertically bending mode (Ni *et al*. 2015) and will be referred as BV1 in this work. The other mode with a frequency of 0.227 Hz is the target of this benchmark study to investigate the mode identifiability and can only be easily distinguished in the vertical FAS for Cases Sam and C2. With the demonstration in the subsequent sections that this mode is principally induced by the motion of the central tower, it is consequently signified as CT. As for the examination of the corresponding transverse FAS, it provides a clear identification for the mode with a frequency of 0.258 Hz under all the excitation cases. This mode has also been identified as the first horizontally bending mode (Ni *et al*. 2015) and will be denoted as BH1. It will be focused on the three major modes (BV1, CT, and BH1) mentioned above to investigate the mode identifiability problem in the current work.

Table 1 Description of 13 known data sets selected under different wind excitation conditions

Condition	Case	Time Duration	Mean Hourly Wind Speed (m/sec)
Normal	N1	15:00-16:00, 28 Dec 1999	2.00
	N2	15:00-16:00, 18 Feb 1999	3.40
	N3	15:00-16:00, 01 Mar 1999	3.34
	N4	15:00-16:00, 21 Jun 1999	3.41
	N5	15:00-16:00, 24 Jul 1999	6.17
	N6	15:00-16:00, 12 Aug 1999	4.20
Typhoon	Maggie	03:00-04:00, 07 Jun 1999	12.11
	Sam	02:00-03:00, 23 Aug 1999	15.62
	York 1	06:00-07:00, 16 Sep 1999	21.72
	York 2	15:00-16:00, 16 Sep 1999	17.91
Critical	C1	08:00-09:00, 07 Jun 1999	7.36
	C2	22:00-23:00, 16 Sep 1999	7.77
	C3	09:00-10:00, 26 Sep 1999	7.43

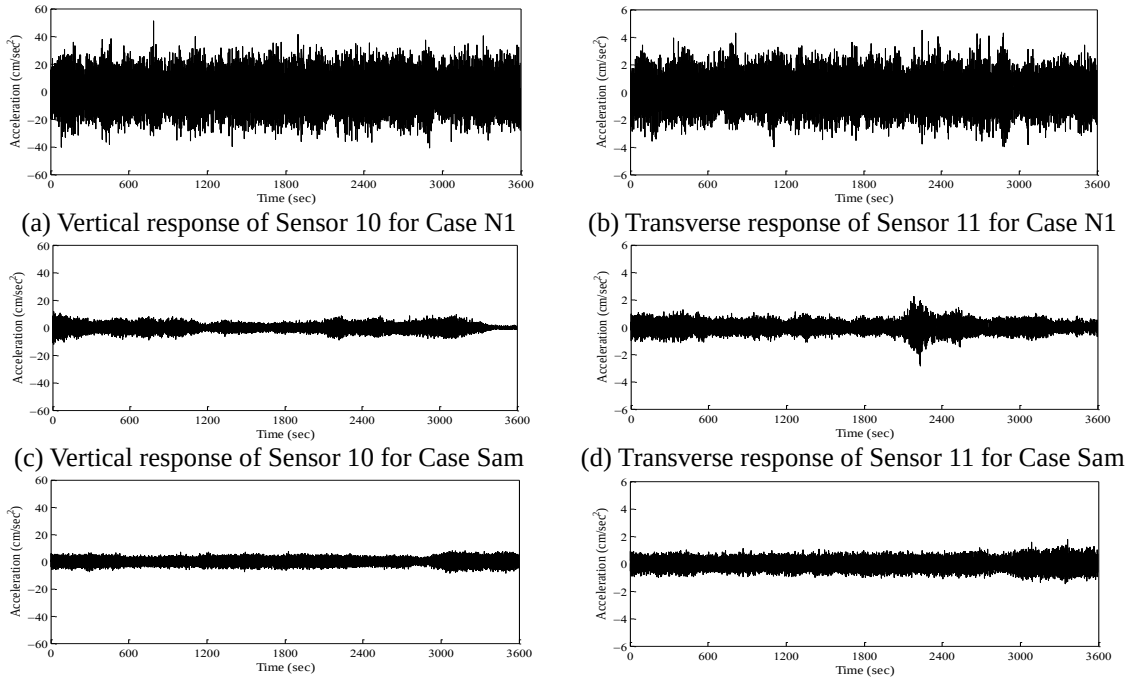

(a) Vertical response of Sensor 10 for Case N1

(b) Transverse response of Sensor 11 for Case N1

(c) Vertical response of Sensor 10 for Case Sam

(d) Transverse response of Sensor 11 for Case Sam

(e) Vertical response of Sensor 10 for Case C2

(f) Transverse response of Sensor 11 for Case C2

Fig. 3 Time histories of Sensors 10 and 11 under different wind conditions

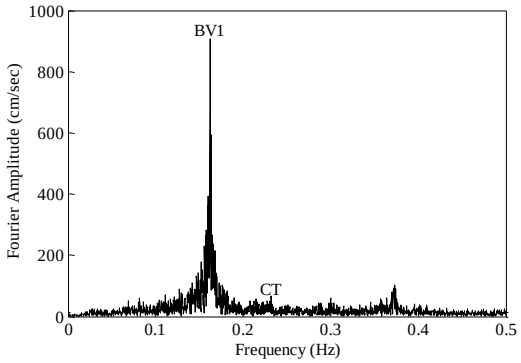

(a) Vertical response of Sensor 10 for Case N1

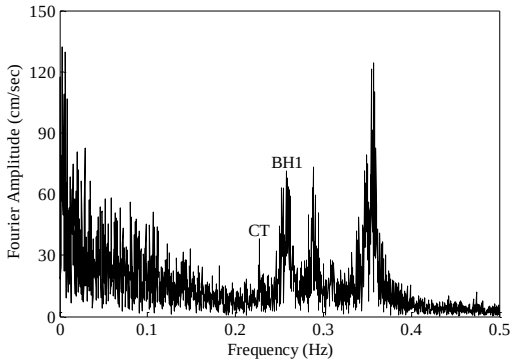

(b) Transverse response of Sensor 11 for Case N1

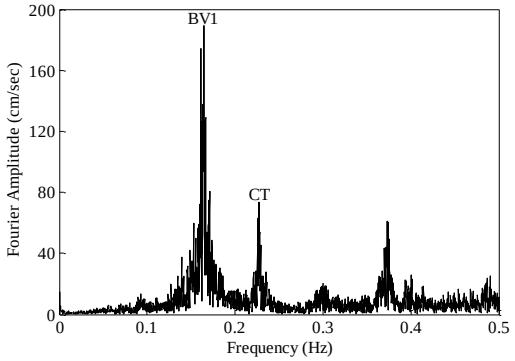

(c) Vertical response of Sensor 10 for Case Sam

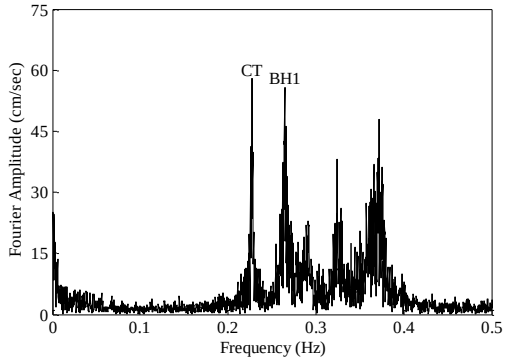

(d) Transverse response of Sensor 11 for Case Sam

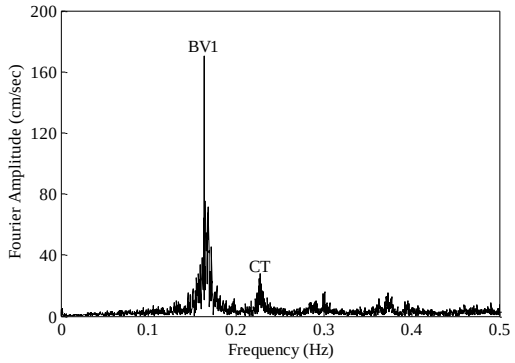

(e) Vertical response of Sensor 10 for Case C2

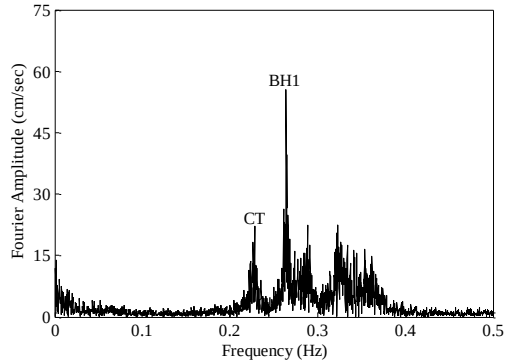

(f) Transverse response of Sensor 11 for Case C2

Fig. 4 Fourier amplitude spectra of Sensors 10 and 11 under different wind conditions

For more extensively comparing the vibration characteristics at all the 24 sensor locations under different excitation conditions, the mean hourly acceleration amplitudes for the 13 sets of known data (and the other 6 sets of blind data) are further computed and plotted in Fig. 5. The mean hourly wind speed for each case is also shown in the same figure with the height of a horizontal line. Again, it is obvious that the vertical acceleration amplitude is larger than the transverse acceleration amplitude at all the eight deck sections for all the different cases. There is

no considerable change in the transverse acceleration amplitude under various wind conditions. The vertical acceleration amplitude, however, is noticeably greater in the cases under the weak wind condition than the cases under the typhoon or critical wind conditions except for Case N2. Considering that the measurement duration of Case N2 falls in the period of Lunar New Year vacation of Hong Kong, the passing traffic perfectly explains the variation in the vertical acceleration amplitude including this exceptional case. It should be particularly noted that the cases under the weak wind condition are usually associated with large vertical acceleration amplitude. On the other hand, the cases under the typhoon or critical wind condition are commonly linked with small vertical acceleration amplitude. With such a high correlation between the wind speed and the vertical vibration amplitude, a question would be naturally raised regarding the adoption of mean hourly wind speed at 7.5 m/sec as the identifiability threshold for mode CT (Ni *et al*. 2015). Is it possible that the mean hourly acceleration amplitude of vertical deck vibration can also serve as an effective threshold? Or the combination of both can create a better index? The unusual case N2 answers part of this question by showing that low vertical vibration amplitude alone would not guarantee the identifiability of mode CT. But, what if the case is the other way around by holding high wind speed together with large vertical vibration amplitude? This exploration to discover the essential factors influencing the identifiability of mode CT will be systematically conducted in the following sections based on the improved SSI algorithm.

4. Improved SSI algorithm for modal parameter identification

In this section, the procedures of the covariance-driven SSI are first reviewed, followed by a brief discussion on its parameter selection. The concepts of alternative stabilization diagram and hierarchical sifting process will also be introduced together with their application to Cases N1, Sam, and C2 under different wind conditions for illustration.

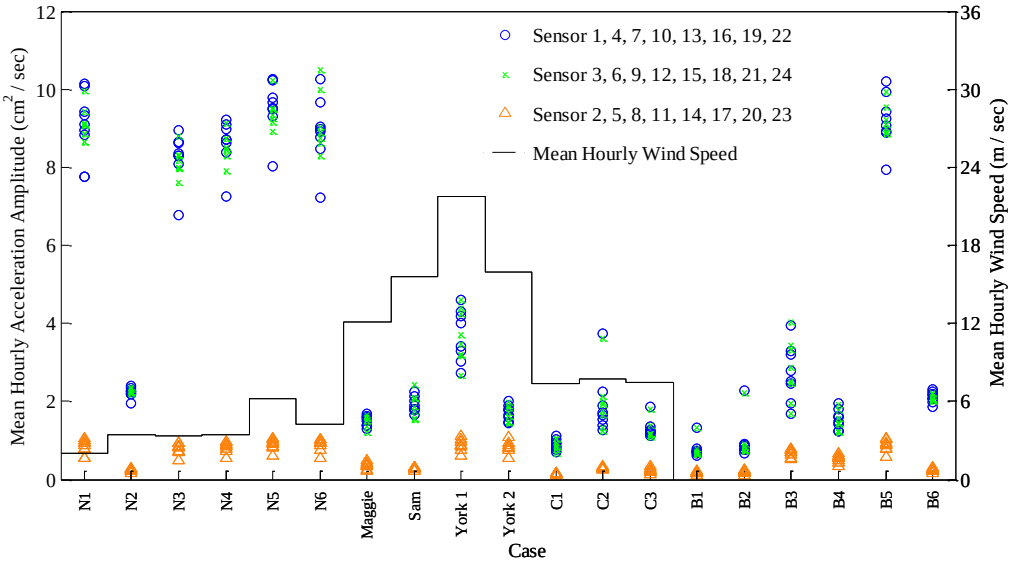

Fig. 5 Mean hourly acceleration amplitudes and mean hourly wind speeds for different cases

4.1 Covariance-driven SSI

If Δt is the sampling time increment and output measurements are conducted to obtain the $l \times 1$ output vector $\mathbf{y}(k)$ at the time instant $k\Delta t$, the $l \times l$ covariance matrix for the output vector at a specified time lag $m\Delta t$ is defined by

$$\mathbf{H}_m = \mathrm{E}[\mathbf{y}(k+m)\mathbf{y}^{\mathrm{T}}(k)] \tag{1}$$

where $\mathrm{E}[\cdot]$ means to take the expected value of the bracketed quantity. Considering the output vectors measured at N consecutive time instants, they can be organized into a Hankel matrix with the selection of a time lag parameter i

$$\mathbf{Y}_{0|2i-1} = \frac{1}{\sqrt{j}}\begin{bmatrix} \mathbf{y}(0) & \mathbf{y}(1) & \cdots & \mathbf{y}(j-1) \\ \mathbf{y}(1) & \mathbf{y}(2) & \cdots & \mathbf{y}(j) \\ \vdots & \vdots & \ddots & \vdots \\ \mathbf{y}(i-1) & \mathbf{y}(i) & \cdots & \mathbf{y}(i+j-2) \\ \hline \mathbf{y}(i) & \mathbf{y}(i+1) & \cdots & \mathbf{y}(i+j-1) \\ \mathbf{y}(i+1) & \mathbf{y}(i+2) & \cdots & \mathbf{y}(i+j) \\ \vdots & \vdots & \ddots & \vdots \\ \mathbf{y}(2i-1) & \mathbf{y}(2i) & \cdots & \mathbf{y}(2i+j-2) \end{bmatrix}_{2il \times j} = \begin{bmatrix} \mathbf{Y}_{0|i-1} \\ \hline \mathbf{Y}_{i|2i-1} \end{bmatrix} = \begin{bmatrix} \mathbf{Y}_p \\ \hline \mathbf{Y}_f \end{bmatrix} \tag{2}$$

where $\mathbf{Y}_p$ and $\mathbf{Y}_f$ are both $il \times j$ with $j = N - 2i + 1$. Post-multiplication of $\mathbf{Y}_f$ by $\mathbf{Y}_p^{\mathrm{T}}$ leads to

$$\begin{aligned} \mathbf{Y}_f\mathbf{Y}_p^{\mathrm{T}} &= \frac{1}{j}\begin{bmatrix} \sum_{k=0}^{j-1}\mathbf{y}(k+i)\mathbf{y}^{\mathrm{T}}(k) & \sum_{k=0}^{j-1}\mathbf{y}(k+i)\mathbf{y}^{\mathrm{T}}(k+1) & \cdots & \sum_{k=0}^{j-1}\mathbf{y}(k+i)\mathbf{y}^{\mathrm{T}}(k+i-1) \\ \sum_{k=0}^{j-1}\mathbf{y}(k+i+1)\mathbf{y}^{\mathrm{T}}(k) & \sum_{k=0}^{j-1}\mathbf{y}(k+i+1)\mathbf{y}^{\mathrm{T}}(k+1) & \cdots & \sum_{k=0}^{j-1}\mathbf{y}(k+i+1)\mathbf{y}^{\mathrm{T}}(k+i-1) \\ \vdots & \vdots & \ddots & \vdots \\ \sum_{k=0}^{j-1}\mathbf{y}(k+2i-1)\mathbf{y}^{\mathrm{T}}(k) & \sum_{k=0}^{j-1}\mathbf{y}(k+2i-1)\mathbf{y}^{\mathrm{T}}(k+1) & \cdots & \sum_{k=0}^{j-1}\mathbf{y}(k+2i-1)\mathbf{y}^{\mathrm{T}}(k+i-1) \end{bmatrix} \\ &\approx \begin{bmatrix} \mathbf{H}_i & \mathbf{H}_{i-1} & \cdots & \mathbf{H}_1 \\ \mathbf{H}_{i+1} & \mathbf{H}_i & \cdots & \mathbf{H}_2 \\ \vdots & \vdots & \ddots & \vdots \\ \mathbf{H}_{2i-1} & \mathbf{H}_{2i-2} & \mathbf{H}_{i+1} & \mathbf{H}_i \end{bmatrix} \end{aligned} \tag{3}$$

Singular value decomposition is then performed on $\mathbf{Y}_f\mathbf{Y}_p^{\mathrm{T}}$ to obtain

$$\mathbf{Y}_f \mathbf{Y}_p^{\mathrm{T}} = \mathbf{USV}^{\mathrm{T}} = \begin{bmatrix} (\mathbf{U}_1)_{il\times 2n} & (\mathbf{U}_2)_{il\times n_1} \end{bmatrix} \begin{bmatrix} (\mathbf{S}_1)_{2n\times 2n} & \mathbf{0}_{2n\times n_1} \\ \mathbf{0}_{n_1\times 2n} & (\mathbf{S}_2)_{n_1\times n_1} \approx \mathbf{0}_{n_1\times n_1} \end{bmatrix} \begin{bmatrix} (\mathbf{V}_1^{\mathrm{T}})_{2n\times il} \\ (\mathbf{V}_2^{\mathrm{T}})_{n_1\times il} \end{bmatrix} \approx \mathbf{U}_1\mathbf{S}_1\mathbf{V}_1^{\mathrm{T}} \quad (4)$$

where n denotes the chosen system order, $n_1 = il - 2n$, $\mathbf{U}$ and $\mathbf{V}$ are orthogonal matrices, and $\mathbf{S}$ is a quasi-diagonal matrix with positive diagonal elements arranged in a decreasing order. By further taking

$$\mathbf{O}_i = \mathbf{U}_1\mathbf{S}_1^{1/2} \quad \text{and} \quad \mathbf{\Gamma}_i = \mathbf{S}_1^{1/2}\mathbf{V}_1^{\mathrm{T}} \quad (5)$$

it has been shown (Peeters 2000) that the discretized system matrix $\mathbf{A}$ in the state space can be determined by

$$\mathbf{A} = \mathbf{O}_i^{\oplus}(1:l(i-1),:)\mathbf{O}_i(l+1:li,:) \quad (6)$$

where the symbol $\oplus$ signifies the pseudo inverse operation. Further with the solved eigenvalues and eigenvectors of $\mathbf{A}$, the modal frequencies ω_k's, the damping ratios ξ_k's, and the mode shape vectors at the output measurement locations $\boldsymbol{\varphi}_k$'s can be directly calculated according to the theory of linear systems. From the above review, it is evident that the time lag parameter i in Eq. (2) and the system order parameter n in Eq. (4) have to be prescribed in conducting the SSI analysis.

4.2 Alternative stabilization diagram

The usually encountered problem for the applications of SSI techniques in large-scale civil structures is that the process noise and measurement noise of a real structure generally do not satisfy all the zero-mean, white-noise, and stationary assumptions on which the derivation of SSI is based. This discrepancy between theoretical simplification and actual complexity would create different degrees of ambiguity in the decision of system order and the identification of corresponding modal parameters. To conquer this difficulty, the SSI technique is typically associated with the stabilization diagram to perform the analysis for practically measured signals from civil structures. More specifically, the time lag parameter i is designated first and then the system order n displayed along the ordinate is gradually increased to identify different sets of modal frequencies plotted along the abscissa. In the stabilization diagram, the actual physical modes can be clearly distinguished from the spurious mathematical modes by the fact that they would basically group together in separated narrow neighborhoods of stable frequency values.

The commercial software equipped with SSI algorithms such as ARTeMIS or MACEC is typically based on the conventional stabilization diagram to perform the modal parameter identification. Several details of choosing the parameters in performing SSI, however, require careful investigation for its successful applications in structures such as high-rise buildings (Faravelli *et al*. 2011) or long-span bridges (Ubertini *et al*. 2013). The authors recently explored the SSI application in stay cables where the conventional stabilization diagram faces a great challenge (Wu *et al*. 2014, 2016). An important discovery is that the lower limit for setting the time lag parameter can be decided by the ratio of the fundamental period of cable to the sampling time increment for a valid identification with the conventional stabilization diagram. Inspired by

such a criterion, that work further proposed an alternative stabilization diagram by fixing the system order *n* first and then varying the time lag parameter *i*. It was suggested to first examine the FAS of cable signals to help an appropriate choice of the system parameter *n* and to determine the fundamental period of cable for setting the lower limit $i_{\min}$ of time lag parameter. In addition, the upper limit of time lag parameter is decided by the need in the subsequent processes to extract reliable modal parameters. It has been validated that the alternative stabilization diagram holds the advantage in less interference from the superfluous modes.

This concept of alternative stabilization diagram is extended to the application for analyzing the vibration measurements of bridge deck in the current study. As mentioned in the previous section, the investigation of the mode identifiability problem will be concentrated on the three major modes (BV1, CT, and BH1) of Ting Kau Bridge. Consequently, the examined frequency range in the following analysis will be focused from 0 to 0.5 Hz. Moreover, the system order is fixed at $n = n_0 = 20$ considering that around 10 peaks can be clearly observed from the FAS of different deck measurements in this frequency range. As illustrated in Fig. 4, the frequency of the first and most dominant mode is about 0.165 Hz (i.e., with a period of 6.1 sec). Considering the sampling frequency at 25.6 Hz (i.e., $\Delta t = 0.039$ sec), $i \geq i_{\min} = 6.1/0.039 \approx 160$ is accordingly taken as the criterion for an appropriate choice of the time lag parameter in this case. Hence, the SSI analysis is then performed with the time lag parameter increasing from $i_{\min} = 160$ to $i_{\max} = i_{\min} + \Delta i = 300$ with the range of $\Delta i = 140$ to establish the alternative stabilization diagrams shown in Figs. 6(a), 6(c), and 6(e) for the three selected cases N1, Sam, and C2 under different wind conditions. The corresponding Fourier amplitude spectra are also shown in the background of these figures. It can be seen that the alternative stabilization diagram of Case N1 is relatively not as clean as those of the other two cases to indicate a little stronger interference from the superfluous modes.

4.3 Hierarchical sifting process

Even enhanced with the alternative stabilization diagram to provide a better foundation for effective modal identification, the task of extracting reliable modal parameters from this diagram requires further efforts. A robust algorithm was also developed in the abovementioned study (Wu *et al*. 2016) to carry out three stages of hierarchical sifting process for gathering close values in all the three caterories of modal parameter including frequencies, damping ratios, and mode shape vectors. With the system parameter fixed at $n = n_0 = 20$ and different values of the time lag parameter taken from $i_{\min} = 160$ to $i_{\max} = i_{\min} + \Delta i = 300$, the conduction of SSI analysis for all these cases would yield $M = n_0 (\Delta i + 1) = 2820$ sets of modal parameters

$$\left(f_k, \xi_k, \boldsymbol{\varphi}_k\right), \quad k = 1, 2, \cdots\cdots, M \tag{7}$$

where the modal frequency $f_k = \omega_k / 2\pi$ is in the unit of Hz. The first stage of hierarchical sifting process starts with sorting all the identified frequency values exhibited in the stabilization diagram in an ascending order

$$f_1 \leq f_2 \leq \cdots\cdots \leq f_{M_1} \tag{8}$$

where M_1 is the number of frequency values falling in the examined frequency range. To

systematically extract the clustered groups of frequency values, a simple clustering index was defined as

$$\Delta f_k = f_{k+L-1} - f_k, \quad k = 1, 2, \cdots\cdots, (M_1 - L + 1) \tag{9}$$

for signifying the span of any adjacent L frequency values. With this operation, the extraction of all the locally clustered frequency values can be conveniently accomplished by merely searching for all the local minima $\Delta f_{k_1}, \Delta f_{k_2}, \cdots\cdots, \Delta f_{k_p}$ from $\Delta f_1, \Delta f_2, \cdots\cdots, \Delta f_{M_1-L+1}$. Certain criterion like

$$\Delta f_{k_m} \le \overline{\Delta f}, \quad m = 1, 2, \cdots\cdots, p \tag{10}$$

can be further imposed to guarantee each extracted group of frequency values would reach a specified level of concentration. With L = 100 and $\overline{\Delta f}$ = 0.005 Hz (1% of the total frequency range examined in the stabilization diagram), a few groups of clustered frequency values as shown in Figs. 6(b), 6(d), and 6(f) can be extracted from Figs. 6(a), 6(c), and 6(e). It is obvious that the somewhat filthy diagrams in Figs. 6(a), 6(c), and 6(e) can be cleaned to produce well clustered groups symbolized by blue cross signs in Figs. 6(b), 6(d), and 6(f) at the end of this stage.

For each group surviving from the first stage, all the damping ratios corresponding to its $L = 100$ frequency values are further sifted in the second stage with the same techniques as adopted in the first stage to filter $L/2$ = 50 most closed values. The $L/2$ = 50 frequency values and their corresponding damping ratios of each mode surviving the second stage finally go to the third stage for examining the consistency of their corresponding mode shape vectors. A consistency index was defined (Wu *et al*. 2016) as

$$\alpha_{km} = \left|\boldsymbol{\varphi}_k - \boldsymbol{\varphi}_m\right|, \quad k, \ m = 1, 2, \cdots\cdots, L/2 \tag{11}$$

where $|\cdot|$ means to take the norm (or length) of the inside vector. It should be especially emphasized that each mode shape vector in Eq. (11) has to be normalized into unit length such that the comparison can be made on the same basis. For each group of L_1 ($L_1 = L/2 = 50$ in the beginning) mode shape vectors, a $L_1 \times L_1$ symmetric consistency matrix with zero diagonal elements can be obtained with the definition of Eq. (11). The average of all the elements in each row (or column) of this consistency matrix except for the diagonal element

$$\overline{\alpha}_k = \frac{1}{(L_1 - 1)} \sum_{m=1, m\neq k}^{L/2} \alpha_{km}, \quad k = 1, 2, \cdots\cdots, L_1 \tag{12}$$

is then adopted to represent the average distance of each normalized mode shape vector to the other $L_1 - 1$ ones in the same group. $\overline{\alpha}_k$ is thus referred as the average distance and used to further carry out the third stage of sifting process on the mode shape vectors. In this work, $\overline{\alpha}_k \le 1\%$ is taken as the shifting criterion. The mode shape vector with the highest $\overline{\alpha}_k$ value above 1% will be deleted one by one until all the remained mode shape vectors satisfy the shifting criterion.

The 50 (or less) normalized shape vectors of modes BV1 and BH1 passing the three stages of sifting are plotted in Fig. 7. The shape vectors of these two modes can be consistently identified under different wind conditions. Figs. 7(a), 7(c), and 7(e) confirm that BV1 is certainly a vertically bending mode with its vertical shape vectors along both sides of deck coincide with each other and its horizontal shape ratios along the central line of deck almost stay at zero. On the other hand, Figs. 7(b), 7(d), and 7(f) validate that BH1 is basically a horizontally bending mode with its vertical shape ratios along both sides of deck much smaller than its horizontal shape ratios along the central line of deck in a full-sine shape. The detailed discussions for the targeted mode CT to explore the mode identifiability problem will be presented in the following sections.

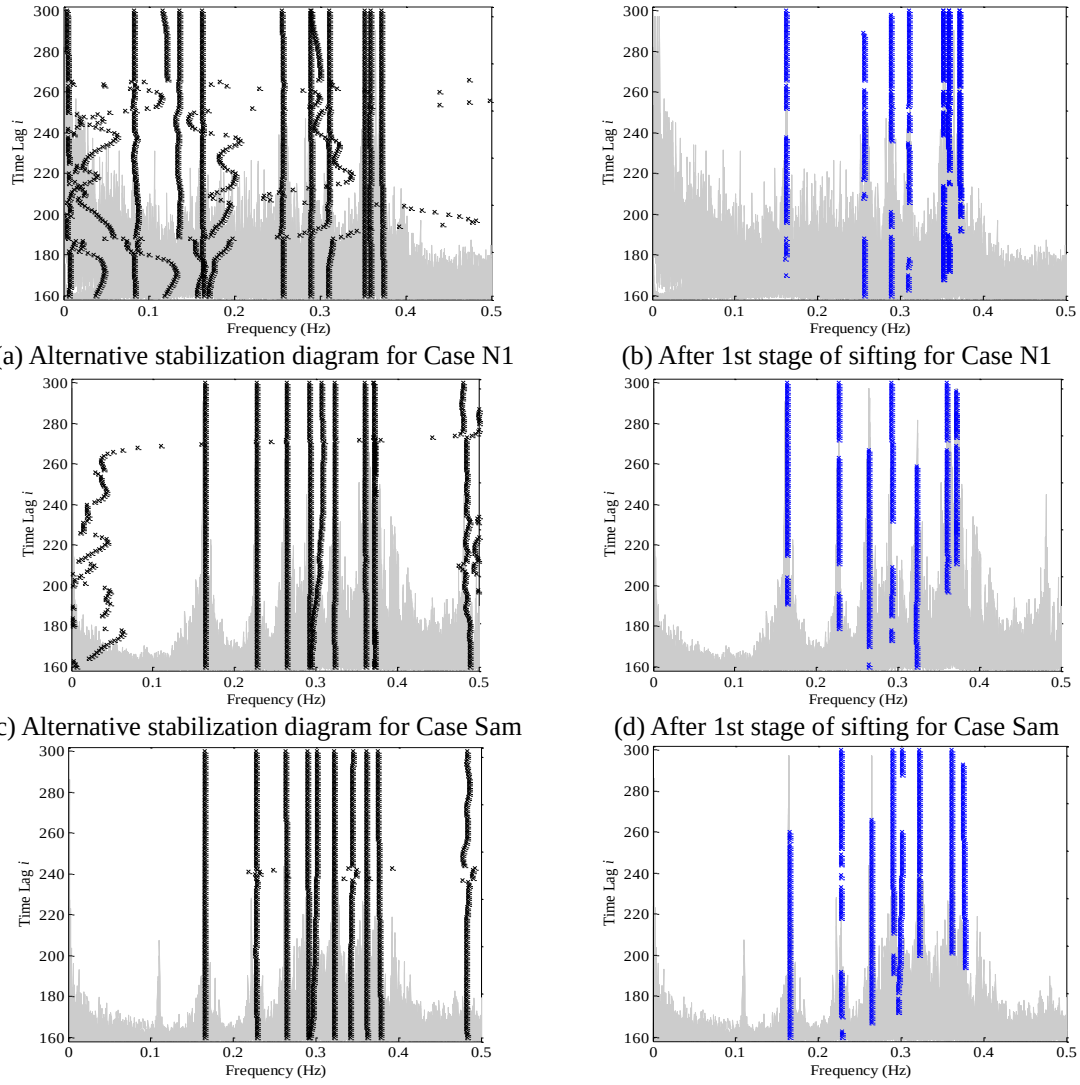

(a) Alternative stabilization diagram for Case N1

(b) After 1st stage of sifting for Case N1

(c) Alternative stabilization diagram for Case Sam

(d) After 1st stage of sifting for Case Sam

(e) Alternative stabilization diagram for Case C2

(f) After 1st stage of sifting for Case C2

Fig. 6 Alternative stabilization diagram and results after 1st sifting stage under different wind conditions

5. SSI analysis for known data sets

Based on the improve SSI algorithm previously described, the analyzed results for all the 13 sets of known data with given wind speed are presented in this section. It should be noticed that the discussion will be focused on modes BV1, CT, and BH1, even though several other modes in the higher frequency range can also be reliably identified with this algorithm.

5.1 Identified modal parameters under different wind conditions

With the improved SSI algorithm to go through all the three sifting stages, the corresponding modal frequencies, damping ratios, and mode shape vectors for the 50 (or less) survivors in each clustered group are then averaged to determine the final identified modal parameters for each mode in this study. The results for Cases N1 to N6 under the normal wind condition are first listed in Table 2. The frequency values of mode BV1 for these 6 cases tightly fall between 0.162 Hz and 0.165 Hz and those of mode BH1 consistently vary from 0.257 Hz to 0.261 Hz. As for the damping ratios, the values of mode BV1 are generally around 1% and those of mode BH1 mainly range from 1% to 2% with an exception close to 4%. Regarding the mode shape vectors for these cases, they are all similar to the ones displayed in Fig. 7. Most important of all, no stable parameters of mode CT can be obtained for all the cases under the normal wind condition as demonstrated in Fig. 6(a).

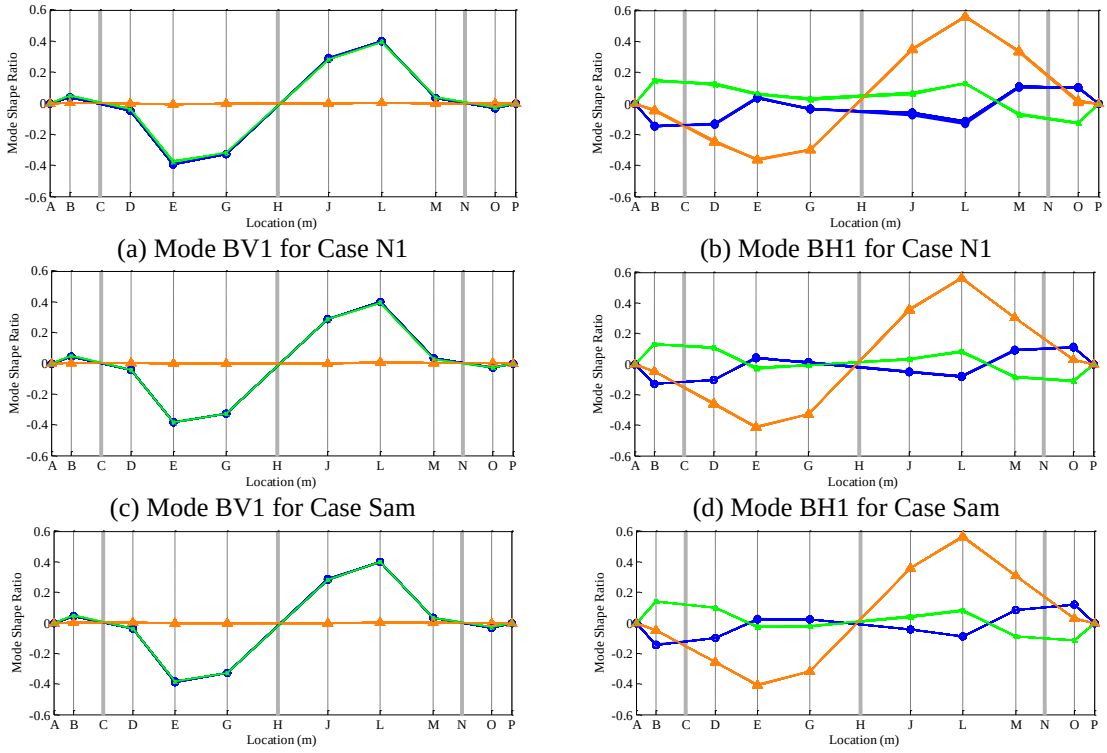

(a) Mode BV1 for Case N1 (b) Mode BH1 for Case N1

(c) Mode BV1 for Case Sam (d) Mode BH1 for Case Sam

(e) Mode BV1 for Case C2 (f) Mode BH1 for Case C2

Fig. 7 Normalized shape vectors of modes BV1 and BH1 under different wind conditions

The identified results for the four cases under the typhoon condition are listed in Table 3. It can be observed that the frequency values of both modes BV1 and BH1 are usually a little larger than the corresponding values identified in the cases under the normal wind condition. A reasonable explanation for this phenomenon is that the much less passing traffic under the strong wind condition would reduce the effective mass of the system to increase the modal frequencies. It is noteworthy that the identified frequencies for the other modes presented in Ni *et al*. (2015) hold the same trend. The identified damping ratios of mode BV1 seems to be higher under the typhoon condition, while this tendency appears to be reversed for mode BH1. Furthermore, the most notable fact is that stable parameters of mode CT can be consistently identified for all the cases under the strong wind condition. The frequency values of this mode closely fall between 0.226 Hz and 0.227 Hz and its damping values are at the order of 0.5%. Combined with the observation under the normal wind condition, mode CT is no doubt a deficient mode that cannot be identified all the time. The 50 (or less) normalized shape vectors of mode CT passing the three stages of sifting for each typhoon case are shown in Fig. 8. For this deficient mode, its vertical shape ratios along both sides of deck distinctly move in the opposite directions to indicate a torsional vibration. Its horizontal shape ratios along the central line of deck, on the other hand, follow a half-sine shape to imply a horizontally bending mode. These two clues disclose that mode CT is a coupled mode in both the torsional and transverse directions, as specified by Ni *et al*. (2015). Further considering the concentration in the central part for major vibration of this mode in both directions and their connected geometry, a more aggressive attempt in this study is to postulate that mode CT is primarily induced by the motion of the central tower. With such a postulation, it would be straightforward to explain the strong influence of the wind condition on the identifiability of this mode. To verify this postulation, the SSI analysis will be conducted in Section 7 with the incorporation of vibration measurements at the central tower.

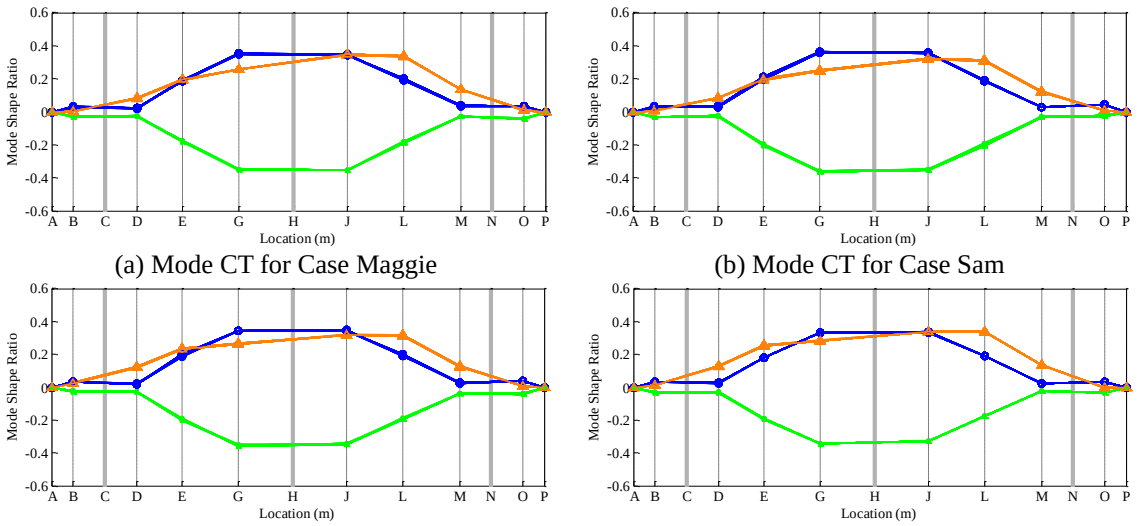

(a) Mode CT for Case Maggie (b) Mode CT for Case Sam

(c) Mode CT for Case York 1 (d) Mode CT for Case York 2

Fig. 8 Normalized shape vectors of mode CT for different typhoon cases

Table 2 Identified modal parameters for normal cases

Case	Mode BV1		Mode CT		Mode BH1	
	Frequency (Hz)	Damping Ratio (%)	Frequency (Hz)	Damping Ratio (%)	Frequency (Hz)	Damping Ratio (%)
N1	0.162	0.848	-	-	0.257	1.797
N2	0.162	1.116	-	-	0.257	1.956
N3	0.163	1.178	-	-	0.259	1.431
N4	0.164	0.853	-	-	0.258	1.227
N5	0.164	1.336	-	-	0.255	3.888
N6	0.165	1.198	-	-	0.261	0.852

Table 3 Identified modal parameters for typhoon cases

Case	Mode BV1		Mode CT		Mode BH1	
	Frequency (Hz)	Damping Ratio (%)	Frequency (Hz)	Damping Ratio (%)	Frequency (Hz)	Damping Ratio (%)
Maggie	0.167	1.544	0.227	0.676	0.263	0.913
Sam	0.164	1.844	0.227	0.317	0.264	0.789
York 1	0.165	3.036	0.227	0.513	0.260	3.894
York 2	0.166	1.671	0.226	0.617	0.260	1.431

Table 4 Identified modal parameters for critical cases

Case	Mode BV1		Mode CT		Mode BH1	
	Frequency (Hz)	Damping Ratio (%)	Frequency (Hz)	Damping Ratio (%)	Frequency (Hz)	Damping Ratio (%)
C1	0.167	1.448	***0.229***	***0.886***	-	-
C2	0.164	1.099	0.228	0.915	0.264	0.719
C3	0.165	0.986	0.227	0.577	0.265	0.951

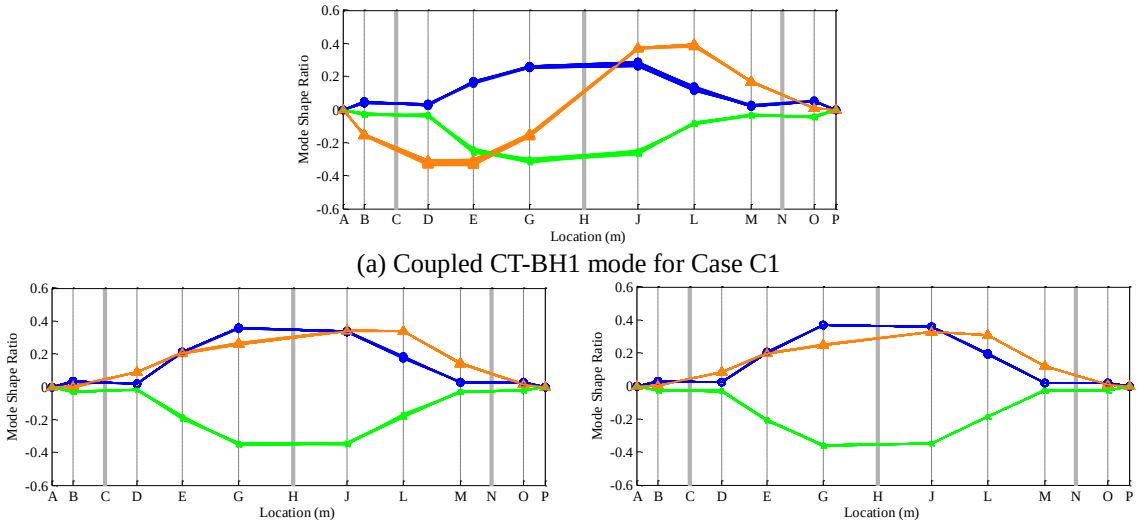

(a) Coupled CT-BH1 mode for Case C1

(b) Mode CT for Case C2

(c) Mode CT for Case C3

Fig. 9 Normalized mode shape vectors of mode CT for critical cases

Finally, the identified modal parameters for the three cases under the critical condition with a mean hourly wind speed close to 7.5 m/sec are listed in Table 4. The results for Cases C2 and C3 are similar to those for the strong wind cases where all the three modes BV1, BH1, and CT can be effectively identified. In Case C1, however, only the parameters of modes BV1 and CT are obtained with a loss of mode BH1. The 50 (or less) normalized shape vectors of mode CT for each critical case are illustrated in Fig. 9. It is found that Fig. 9(b) and 9(c) for Cases C2 and C3 exhibit similar shape vectors of mode CT as those demonstrated in Fig. 8 for typhoon cases. But surprisingly, the mode shape vector shown in Fig. 9(a) for Case C1 seems to be a combination of modes CT and BH1. More specifically, its vertical shape ratios along both sides of deck hold the characteristics of mode CT and its horizontal shape ratios along the central line of deck follow a full-sine shape as in mode BH1. This observation indicates the possibility that the two closely-spaced modes CT and BH1 may be further coupled under certain critical case and explains the disappearance of mode BH1.

5.2 Effect of traffic excitation

Based on the discussions in the previous subsection, it is evident that the identifiability of mode CT strongly depends on the wind excitation. But with the high correlation between the wind excitation and the traffic excitation in a negative manner, it is necessary to clarify the effect of traffic excitation on the identifiability of mode CT. In other words, the two typical cases under strong wind with light traffic and under weak wind with heavy traffic have been extensively investigated. It would be instructive to further explore the case under strong wind with heavy traffic and that under weak wind with light traffic. It is very difficult, if not impossible, to extract 1-hour acceleration records for these two special cases rarely occurred in real situations. From the

13 sets of available data sets, two durations of 5-minute acceleration records are deliberately selected for this assessment.

First, the acceleration records extracted from 33 to 38 minutes of Case York 1 are adopted to represent the case under strong wind with heavy traffic. Their corresponding time histories and FAS for Sensors 10 and 11 are depicted in Fig. 10. The mean wind speed in this duration is 17.82 m/sec and belongs to the strong wind condition. The mean vertical acceleration amplitude in this case is 5.4 m/sec^2 to falls between those of typical weak wind (heavy traffic) and strong wind (light traffic) cases according to Fig. 5. It is found that mode CT cannot be identified with the improved SSI algorithm. The Fourier amplitude spectra displayed in Figs. 10(c) and 10(d) show their similarity to Figs. 4(a) and 4(b) for the weak wind (heavy traffic) case. Consequently, it indicates that heavy traffic excitation will obstruct the identifiability of mode CT even under the typhoon condition to produce stronger vibration of the central tower. Comparison of the FAS in Figs. 4(a), 4(c), and 4(e) provides more evidences to explain this phenomenon. The heavy passing traffic on the bridge deck would provoke a dominant contribution from mode BV1 to reduce the relative identifiability of mode CT. Next, the acceleration records extracted from 20 to 25 minutes of Case N2 are utilized to study the case under weak wind with light traffic. Their corresponding time histories and FAS for Sensors 10 and 11 are plotted in Fig. 11. The mean wind speed in this duration is 3.31 m/sec under the weak wind condition and the mean vertical acceleration amplitude in this case is 1.5 m/sec^2 to fall in the same order as that of a typical strong wind (light traffic) case. Again, mode CT cannot be identified with the improved SSI algorithm in this case. The Fourier amplitude spectra displayed in Figs. 11(c) and 11(d) also demonstrate that modes BV1 and BH1 are blurred due to the lack of passing traffic to enhance the contribution from both modes.

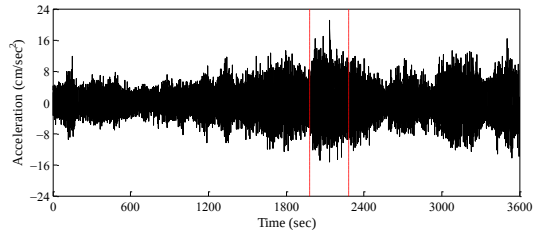

(a) Vertical response of Sensor 10 for Case York 1

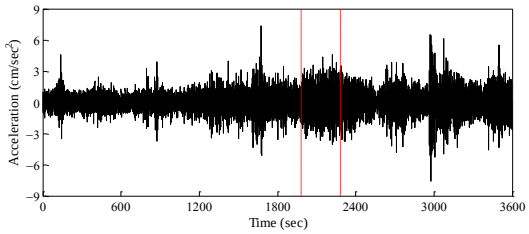

(b) Horizontal response of Sensor 11 for Case York 1

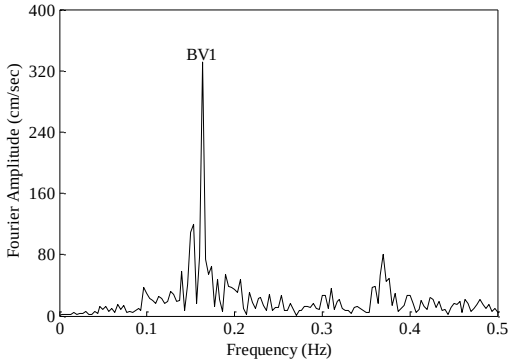

(c) FAS of Sensor 10 for Case York 1

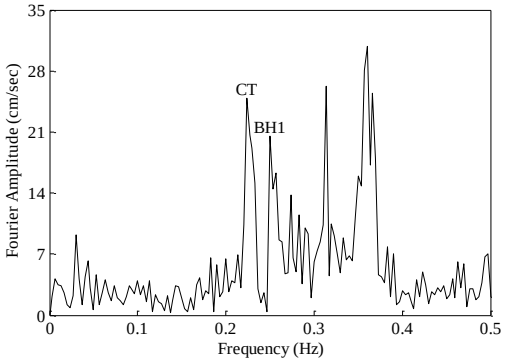

(d) FAS of Sensor 11 for Case York 1

Fig. 10 Extracted time histories and Fourier amplitude spectra of Sensors 10 and 11 for Case York 1

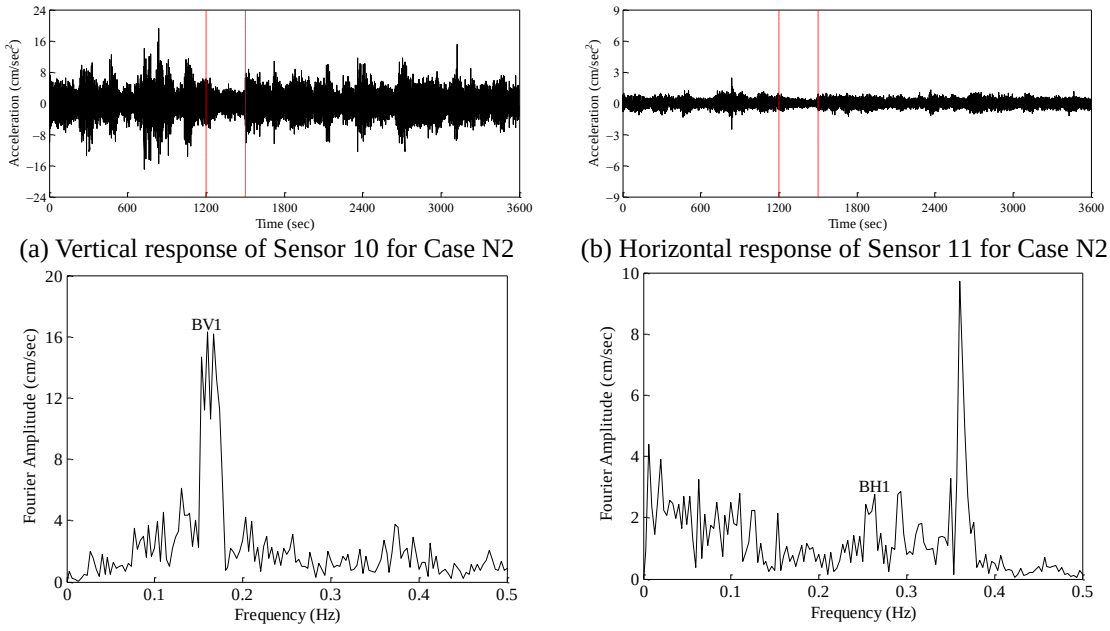

(a) Vertical response of Sensor 10 for Case N2

(b) Horizontal response of Sensor 11 for Case N2

(c) FAS of Sensor 10 for Case N2

(d) FAS of Sensor 11 for Case N2

Fig. 11 Extracted time histories and Fourier amplitude spectra of Sensors 10 and 11 for Case N2

The evaluation of these two additional cases elucidates that the identiability of mode CT is related to both the wind and traffic excitations. A threshold for the mean wind speed was determined as larger than 7.5 m/sec (Ni *et al*. 2015). Another threshold for the mean vertical acceleration amplitude at deck is further proposed in this work to be less than 4 m/sec^2 based on the observations from Fig. 5. Both thresholds need to be concurrently satisfied to ensure a reliable identification of mode CT. A critical case can be called if either the wind or traffic excitation level falls in the neighborhood of its own threshold. From this point of view, Cases C1 to C3 (critical wind speed) together with Case York 1 (critical vertical deck acceleration) should all be considered as critical cases.

6. Analysis for blind data sets

To validate the methodology established in this work, 6 sets of blind data without given wind excitation conditions are analyzed in this section. A preliminary analysis is first performed on Cases B1 to B6 by portraying their Fourier amplitude spectra of Sensors 10 and 11 in Fig. 12. Comparison of the FAS in Fig. 12 with those shown in Fig. 4 may at least unveil the partial faces of these 6 blind cases. First of all, mode CT can be clearly distinguished in the vertical FAS for Cases B1 to B4. This implies that these four cases should be under either the strong wind or critical condition. Cases B5 and B6, on the other hand, naturally fall into the category under the weak wind condition. Furthermore, the stronger contribution from mode CT relative to that of mode BV1 as shown in Fig. 12 may suggest Cases B1 and B2 to be under the strong wind

condition by comparing to the similar trend in Fig. 4. With the additional information of mean acceleration amplitudes for these 6 sets of blind data also illustrated in Fig. 5, the high vibration amplitude in the vertical direction directly exposes Case B5 to be under the weak wind (heavy traffic) condition. In addition, Case B6 would be suspected to be like Case N2 under weak wind and light traffic excitations with its relatively low vibration amplitude and hostility to the identification of mode CT. The identified results with the improved SSI algorithm for the 6 blind cases are listed in Table 5. With no surprise, mode CT cannot be identified for Cases B5 and B6 supposed to be under the weak wind condition. In addition, the identified frequency values of both modes BV1 and BH1 are mostly a little larger in Cases B1 to B4 than those in Cases B5 and B5. This is also an indication that the former 4 cases are under either the strong or critical wind condition. In Fig. 13, the 50 (or less) normalized shape vectors of modes CT and BH1 after three stages of sifting for Cases B1 to B4 are depicted. For Case B3, the parameters of mode BH1 cannot be identified and the mode shape vector shown in Fig. 13(e) corresponds to a combination of modes CT and BH1. Similar to Case C1 discussed in the previous section, this suggests that the two closely-spaced modes CT and BH1 are coupled together and Case B3 is under the critical condition.

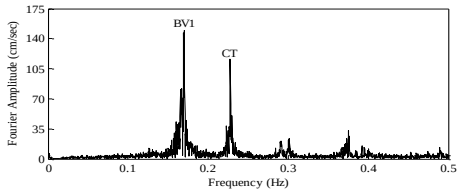

(a) FAS of Sensor 10 for Case B1

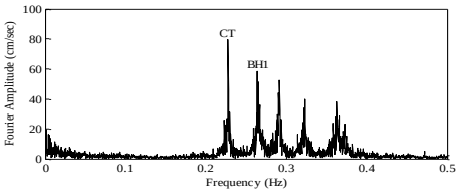

(b) FAS of Sensor 11 for Case B1

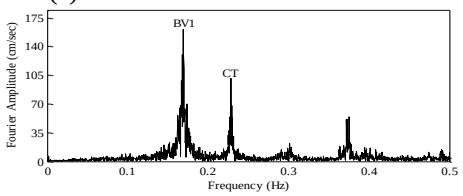

(c) FAS of Sensor 10 for Case B2

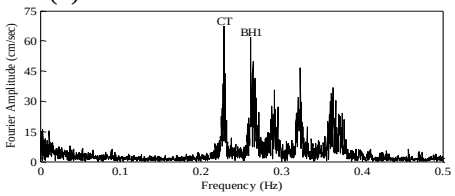

(d) FAS of Sensor 11 for Case B2

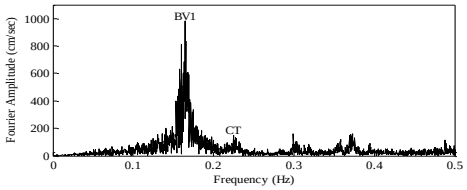

(e) FAS of Sensor 10 for Case B3

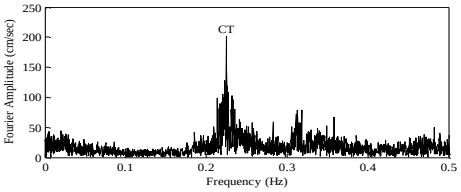

(f) FAS of Sensor 11 for Case B3

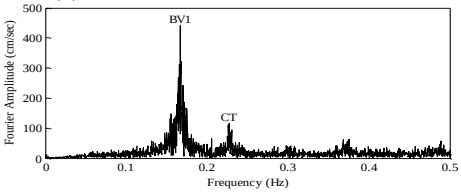

(g) FAS of Sensor 10 for Case B4

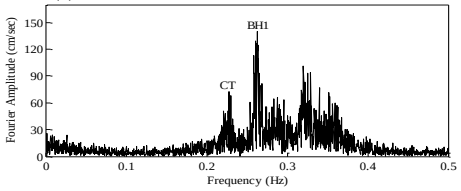

(h) FAS of Sensor 11 for Case B4

Continued-

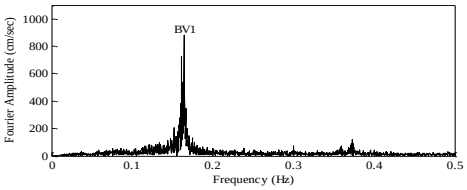

(i) FAS of Sensor 10 for Case B5

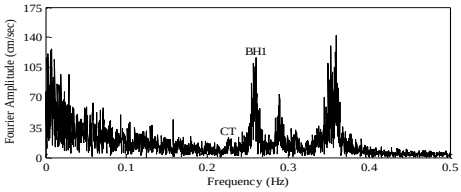

(j) FAS of Sensor 11 for Case B5

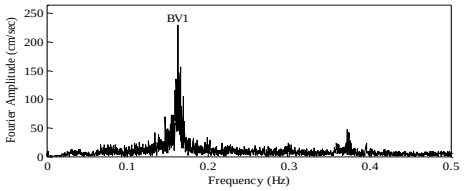

(k) FAS of Sensor 10 for Case B6

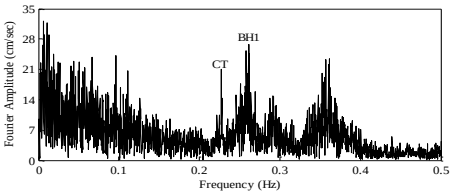

(l) FAS of Sensor 11 for Case B6

Fig. 12 Fourier amplitude spectra of Sensors 10 and 11 for different blind cases

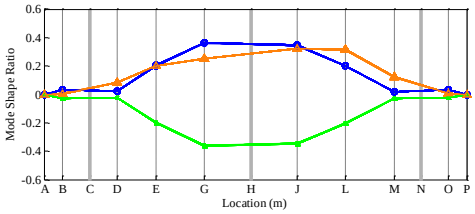

(a) Mode CT for Case B1

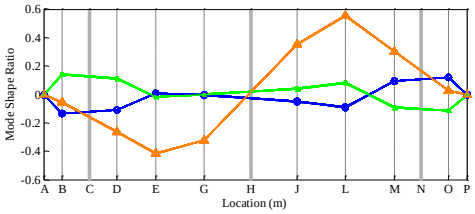

(b) Mode BH1 for Case B1

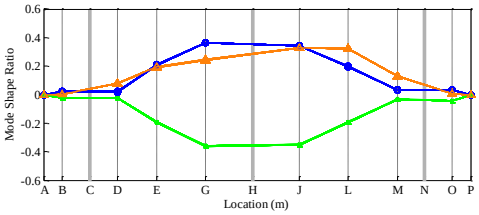

(c) Mode CT for Case B2

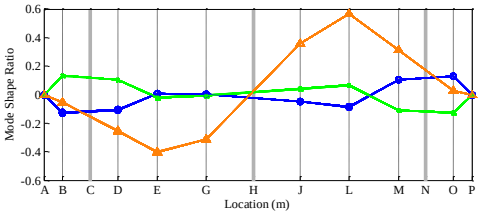

(d) Mode BH1 for Case B2

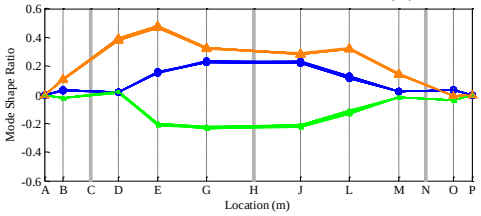

(e) Coupled CT-BH1 mode for Case B3

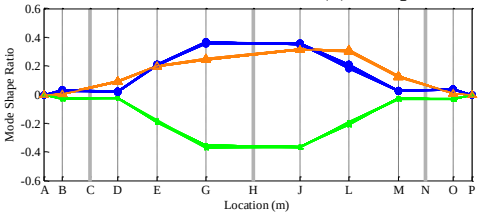

(f) Mode CT for Case B4

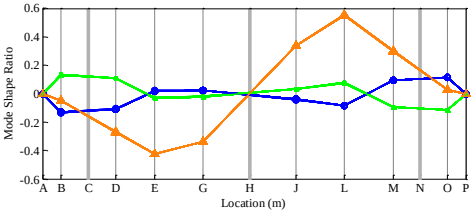

(g) Mode BH1 for Case B4

Fig. 13 Normalized shape vectors of modes CT and BH1 for different blind cases

Table 5 Identified modal parameters for blind data

Case	Mode BV1		Mode CT		Mode BH1	
	Frequency (Hz)	Damping Ratio (%)	Frequency (Hz)	Damping Ratio (%)	Frequency (Hz)	Damping Ratio (%)
B1	0.169	0.778	0.227	0.343	0.265	0.558
B2	0.169	1.079	0.228	0.414	0.264	0.602
B3	0.165	2.243	***0.228***	***1.953***	-	-
B4	0.166	1.676	0.228	1.777	0.262	0.902
B5	0.163	0.894	-	-	0.258	1.192
B6	0.166	1.604	-	-	0.256	2.491

7. Analysis further incorporating measurements at central tower

Based on close examination on the geometry of its mode shape vector, it is postulated in Section 5 that the deficient mode CT is principally induced by the motion of the central tower. To certify this postulation, the analysis with further incorporation of the acceleration records measured at the central tower is performed in this section. As illustrated in Fig. 1, two bi-axial accelerometers labeled as T1 and T2 in this work are installed at the top and the base of the central tower, respectively. The measurements of Sensors T1 and T2 in the transverse (y) direction are taken to conduct the analysis together with the records from the 24 uni-axial accelerometers deployed on the bridge deck. It should be mentioned that only the acceleration records of Sensors T1 and T2 corresponding to Cases N1 to N6 and the four typhoon cases are currently available for this investigation.

Taking Case N1 and Case Sam as examples, the transverse time histories of Sensors T1 and T2 and their corresponding FAS are first displayed in Figs. 14 and 15, respectively. It is interesting to observe that the general vibration amplitudes at both tower locations are relatively larger in Case N1 under the weak wind condition than those in Case Sam under the strong wind condition. This situation is reasonable by considering that the tower vibration can be induced both by the direct wind excitation and the indirect traffic excitation through connected stay cables. The significant contribution from the passing traffic under the weak wind condition may cause larger vibration responses than those mainly induced by the wind excitation under the strong wind condition. This argument can be further supported by the results in the frequency domain. The more prominent higher modes under the weak wind condition imply that its excitation is with the content in a higher frequency range, possibly from traffic. But more importantly, mode CT with a frequency value of 0.227 Hz dominantly appears in the FAS of different tower measurements in both cases to confirm that the major motion of this mode locates at the central tower rather than at the bridge deck.

More solid evidences can be collected from performing the SSI analysis with both the deck and tower measurements to prove that mode CT is more a tower mode than a deck mode. The identified modal parameters for the 6 cases under the weak wind condition are listed in Table 6. In

contrast to Table 2 obtained from performing the SSI analysis simply with the deck measurements, stable parameters of mode CT can be identified for all the cases under the weak wind condition. In other words, mode CT can no longer be considered as a deficient mode with the addition of two tower measurements. The 50 (or less) extended shape vectors of mode CT to include the shape ratios at two tower locations for Cases N1 to N6 and the four typhoon cases are also drawn in Fig. 16. The in-scale plots in Fig. 16 evidently demonstrate that the dominance of tower motion at the top for mode CT. More specifically, the largest shape ratio at deck for this mode is merely around 14% of that at the tower top in the four typhoon cases with consistent mode shape vectors. As for the 6 cases under the weak wind conditions, the mode shape ratios at deck locations may mildly change in different cases compared to the corresponding steady values at tower locations. More precisely, the transverse mode shape ratios along the central line of deck are relatively more stable than the vertical mode shape ratios at both sides of deck in these cases. Even though the tower measurements corresponding to Cases C1, C2, and C3 are not available, the extended mode shape vectors of mode CT for these three cases can be expected to be similar to Fig. 9 with the addition of the steady tower components demonstrated in all the cases of Fig. 16. All the above observations point to the direction that an effective consideration of mode CT should cover both the tower and deck components of this bridge. To clearly express the vibration mechanism of this mode, it can be conveniently pictured as the transversely bending motion of the central tower to simultaneously induce the transversely bending and torsional motions of the connected deck.

Table 6 Identified modal parameters for normal cases including pylon measurement

Case	Mode BV1		Mode CT		Mode BH1	
	Frequency (Hz)	Damping Ratio (%)	Frequency (Hz)	Damping Ratio (%)	Frequency (Hz)	Damping Ratio (%)
N1	0.162	0.885	0.227	0.472	0.257	1.612
N2	0.162	1.018	0.226	0.761	0.258	1.724
N3	0.163	0.164	0.226	0.678	0.259	1.285
N4	0.164	0.985	0.224	1.594	0.258	1.043
N5	0.164	1.489	0.225	1.125	0.257	4.527
N6	0.165	1.163	0.226	1.850	0.261	0.806

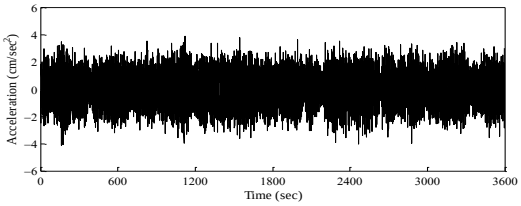

(a) Transverse response of Sensor T1 for Case N1

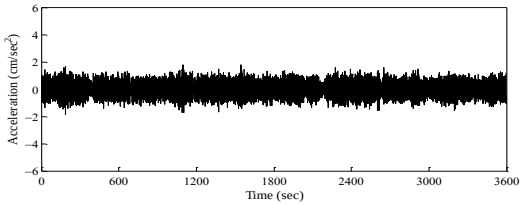

(b) Transverse response of Sensor T2 for Case N1

Continued-

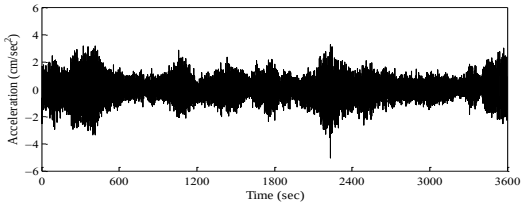

(c) Transverse response of Sensor T1 for Case Sam

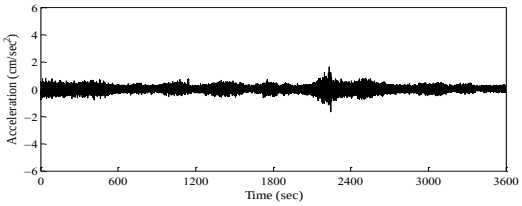

(d) Transverse response of Sensor T2 for Case Sam

Fig. 14 Transverse time histories of Sensors T1 and T2 under different wind conditions

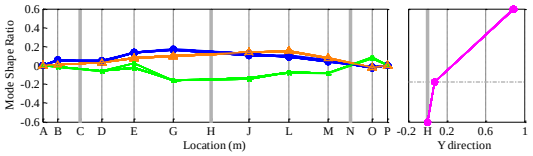

(a) Mode CT for Case N1

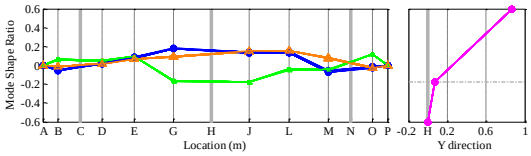

(b) Mode CT for Case N2

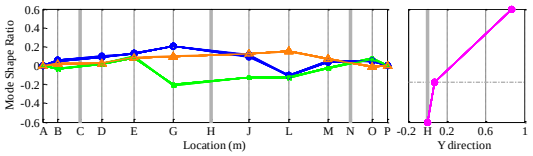

(c) Mode CT for Case N3

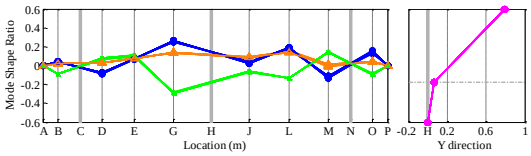

(d) Mode CT for Case N4

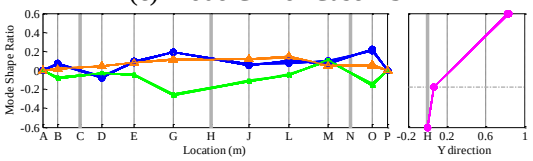

(e) Mode CT for Case N5

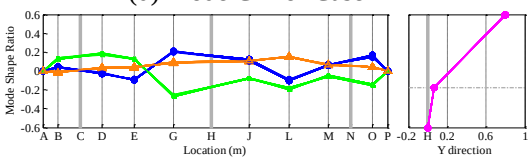

(f) Mode CT for Case N6

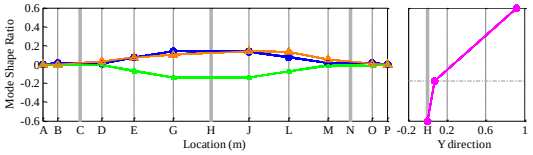

(g) Mode CT for Case Maggie

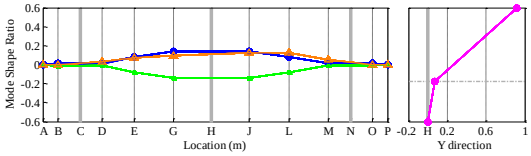

(h) Mode CT for Case Sam

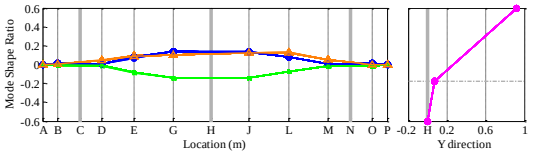

(i) Mode CT for Case York 1

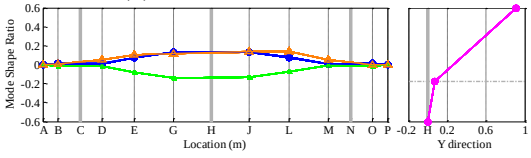

(j) Mode CT for Case York 2

Fig. 16 Extended mode shape vectors of mode CT for different wind conditions

8. Conclusions

Focused on a deficient mode that cannot be always identified from the monitoring data of Ting Kau Bridge under different wind conditions, a benchmark study is launched to explore the mode identifiability in conducting the operational modal analysis with ambient vibration measurements. For systematically assessing this problem, a recently developed SSI algorithm based on an alternative stabilization diagram and a hierarchical sifting process is extended and applied in this research to investigate several sets of known and blind monitoring data. The evaluation of delicately selected cases clearly distinguishes the effect of traffic excitation on the identifiability of the targeted deficient mode from the effect of wind excitation. An additional upper limit for the vertical acceleration amplitude at deck, mainly induced by the passing traffic, is subsequently suggested to supplement the previously determined lower limit for the wind speed. Both thresholds need to be simultaneously satisfied to ensure a reliable identification of the deficient mode. The strong wind excitation increases the own contribution from the deficient mode in output measurements, while the light traffic excitation alleviates the contributions from the other possibly dominant modes. From a more general perspective, this finding illuminates the above two key features in input excitations to magnify the identifiability of any specific mode.

Further efforts are dedicated in the present work to carefully inspect the shape vector of the deficient mode under different excitation conditions. Such an examination leads to the postulation that this mode is actually induced by the motion of the central tower. This postulation explains the strong dependence of identifiability on the wind excitation for the deficient mode, which is not supposed to occur in the modes majorly with deck vibration. The SSI analysis incorporating the tower measurements solidly verifies this postulation by yielding the prevailing components at the tower locations in the extended mode shape vector. Moreover, it is also confirmed that this mode can be stably identified under all the circumstances with the addition of tower measurements to remove the tag of deficient mode. An important lesson learned from this discovery is that the problem of mode identifiability usually comes from the lack of appropriate measurements taken at the right locations. However, the choice of proper sensor locations to robustly identify specific modes under different conditions may require deliberate efforts to grasp the vibration characteristics of the investigated system. This benchmark study on mode identifiability provides an excellent forum to address these critical issues in structural health monitoring.

Acknowledgments

The authors would like to express their sincere appreciations to Prof. Yi-Qing Ni and Mr. You-Wu Wang of Hong Kong Polytechnic University for the efforts in launching this benchmark problem and preparing the monitoring data. This research is supported by the Ministry of Science and Technology of Republic of China under Grant NSC102-2221-E-224-043 and Grant MOST103-2221-E-224-008.

References

Alicioglu, B. and Lus, H. (2008), "Ambient vibration analysis with subspace methods and automated mode selection: case studies", *J. Struct. Eng. - ASCE*, **134**(6), 1016-1029.

Bakir, P.G. (2011), "Automation of the stabilization diagram for subspace based system identification", *Expert Syst. Appl.*, **38**(12), 14390-14397.
Bendat, J.S. and Piersol, A.G. (1986), *Random Data: Analysis and Measurement Procedures*, John Wiley & Sons, New York, USA.
Brinker, R., Zhang, L. and Andersen, P. (2001), "Modal identification of output-only systems using frequency domain decomposition", *Smart Mater. Struct.*, **10**(3), 441-445.
Carden, E.P. and Brownjohn J.M. (2008), "Fuzzy clustering of stability diagrams for vibration-based structural health monitoring", *Comput.-Aided Civil Infrastruct. Eng.*, **23**(5), 360-372.
Faravelli, L., Ubertini, F. and Fuggini, C. (2011), "System identification of a super high-rise building via a stochastic subspace approach", *Smart Struct. Syst.*, **7**(2), 133-152.
Jacobsen, N.J., Andersen, P. and Brincker, R. (2006), "Using enhanced frequency domain decomposition as a robust technique to harmonic excitation in operational modal analysis", *Proceedings of the ISMA Conference on Advanced Acoustics and Vibration Engineering*, Leuven, Belgium, September.
Juang, J.N. and Pappa, R.S. (1985), "An eigensystem realization algorithm for modal parameter identification and model reduction", *J. Guid. Control Dynam.*, **8**(5), 620-627.
Ko, J.M. and Ni, Y.Q. (2005), "Technology developments in structural health monitoring of large-scale bridges", *Eng. Struct.*, **27**(12), 1715-1725.
Ljung, L. (1987), *System Identification: Theory for the User*, Prentice-Hall, Englewood Cliffs, New Jersey, USA.
Ni, Y.Q., Wong, K.Y. and Xia, Y.X. (2011), "Health checks through landmark bridges to sky-high structures", *Adv. Struct. Eng.*, **14**(1), 103-119.
Ni, Y.Q., Wang, Y.W. and Xia, Y.X. (2015), "Investigation of mode identifiability of a cable-stayed bridge: comparison from ambient vibration responses and from typhoon-induced dynamic responses", *Smart Struct. Syst.*, **15**(2), 447-468.
Parloo, E., Guillaume, P., Cauberghe, B. (2003), "Maximum likelihood identification of non-stationary operational data", *J. Sound Vib.*, **268**(5), 971-991.
Peeters, B. (2000), "System identification and damage detection in civil engineering", Ph.D. Dissertation, Katholieke Universiteit Leuven, Leuven.
Peeters, B. and De Roeck G. (1999), "Reference-based stochastic subspace identification for output-only modal analysis", *Mech. Syst. Signal Pr.*, **13**(6), 855-878.
Reynders, E., Houbrects, J. and De Roeck, G. (2012), "Fully automated (operational) modal analysis", *Mech. Syst. Signal Pr.*, **29**, 228-250.
Scionti, M. and Lanslots, J.P. (2005), "Stabilisation diagrams: pole identification using fuzzy clustering techniques", *Adv. Eng. Softw.*, **36**(11), 768-779.
Ubertini, F., Gentile, C. and Materazzi, A.L. (2013), "Automated modal identification in operational conditions and its application to bridges", *Eng. Struct.*, **46**, 264-278.
Van Overschee, P. and De Moor, B. (1991), "Subspace algorithm for the stochastic identification problem", *Proceedings of the 30th IEEE Conference on Decision and Control*, Brighton, England, December.
Van Overschee, P. and De Moor, B. (1993), "Subspace algorithms for the stochastic identification problem", *Automatica*, **29**(3), 649-660.
Van Overschee, P. and De Moor, B. (1996), *Subspace Identification for Linear Systems: Theory-Implementation-Applications*, Kluwer Academic Publishers, Dordecht, Netherlands.
Wong, K.Y. (2004), "Instrumentation and health monitoring of cable-supported bridges", *Struct. Control Health Monit.*, **11**(2), 91-124.
Wong, K.Y. (2007), "Design of a structural health monitoring system for long-span bridges", *Struct. Infrastruct. E.*, **3**(2), 169-185.
Wu, W.H., Chen, C.C., Wang, S.W. and Lai, G. (2014), "Modal parameter determination of stay cable with an improved algorithm based on stochastic subspace identification", *Proceedings of 7th European Workshop on Structural Health Monitoring*, Nantes, France, July.
Wu, W.H., Wang. S.W., Chen, C.C. and Lai, G. (2016), "Application of stochastic subspace identification for stay cables with an alternative stabilization diagram and hierarchical sifting process", *Struct. Control*

Health Monit., in press (DOI: 10.1002/stc.1836).